

Supplementary Information:

Electrodeposited $\text{Ni}_x\text{Co}_{3-x}\text{O}_4$ nanostructured films as bifunctional oxygen electrocatalysts

Timothy N. Lambert,^{*a} Julian A. Vigil,^a Suzanne E. White,^a Danae J. Davis,^a Steven J. Limmer,^b Patrick D. Burton,^c Eric N. Coker,^d Thomas E. Beechem,^e Michael T. Brumbach^f

^{*}Department of Materials, Devices & Energy Technologies, Sandia National Laboratories, Albuquerque, New Mexico, 87185, USA, Fax: 505 844 7786; Tel: 505 284 6967; E-mail: tnlambe@sandia.gov.

^a Department of Materials, Devices, and Energy Technologies

^b Physics Based Microsystems

^c Chemical and Biological Systems

^d Advanced Materials Laboratory

^e Nanoscale Sciences Department

^f Materials Characterization and Performance

* Author to whom correspondences should be addressed

Abbreviations used here:

EDS = Energy dispersive spectroscopy

SEM = Scanning electron microscopy

TEM = Transmission electron microscopy

PXRD = Powder x-ray diffraction

JCPDS = Joint Committee on Powder Diffraction Standards

XPS = X-ray photoelectron spectroscopy

TGA = Thermogravimetric analysis

DSC = Differential scanning calorimetry

ORR = Oxygen reduction reaction

OER = Oxygen evolution reaction

ECSA = Electrochemically active surface area

Experimental

General

All chemicals were obtained commercially and used as received, without further purification. Cobalt (II) nitrate hexahydrate ($\text{Co}(\text{NO}_3)_2 \cdot 6\text{H}_2\text{O}$) was purchased from Alfa Aesar. Sodium nitrate (NaNO_3) was purchased from Fisher Scientific. Nickel (II) nitrate hexahydrate ($\text{Ni}(\text{NO}_3)_2 \cdot 6\text{H}_2\text{O}$) was purchased from Acros Organics. Ethyl alcohol was purchased from Pharmco-Aaper. Nickel foil (0.05 mm thick, 99+% metals basis) was purchased from Alfa Aesar.

Materials Characterization.

Grazing-Incidence X-ray Diffraction (GIXRD). A Siemens model D500 θ - 2θ powder diffractometer (Bruker AXS, Inc. Madison, WI) was used for GIXRD data collection with samples maintained at room temperature (25°C). Copper $\text{K}\alpha$ (0.15418 nm) radiation was produced via a sealed-tube X-ray source and a diffracted-beam curved graphite monochromator; a conventional scintillation counter was used as the detector. Fixed 0.3° incident beam and scatter slits were used (goniometer radius = 120 mm), and the instrument power settings were 40 kV and 30 mA. A series of powder diffraction patterns were collected using grazing angles of 0.5°, 1.0°, 1.5° and 2.0° θ . The patterns were collected using the following parameters: 10-80° 2θ range, step-size of 0.05° 2θ and a count time of 30 seconds. Crystallite size was determined using the Scherrer equation with the (220) peak.

Scanning Electron Microscopy (SEM). The samples were imaged using a Zeiss Supra 55VP field emitter gun scanning electron microscope (FEGSEM).

Raman Spectroscopy. Spectra were collected using a WiTec alpha 300R system employing 532 nm laser light. Spot sizes were approximately 600 nm with powers selected to ensure sample heating to less than 30 K. Spectral resolution is $\pm 1 \text{ cm}^{-1}$. No spatial variation was observed in any of the films.

X-ray Photoelectron Spectroscopy. Powders and thin-film electrode samples were analyzed via XPS at pressures less than $5 \cdot 10^{-9}$ Torr. XPS was performed using a Kratos Axis Ultra DLD instrument using monochromatic Al $\text{K}\alpha$ (1486.7 eV) source. The analysis area was an elliptical spot size of 300 x 700 microns. Several locations on each sample were analyzed to obtain a representative sampling. Survey spectra were recorded

with an 80 eV pass energy, 500 meV step sizes, and 100 ms dwell times. High resolution spectra were recorded with a 20 eV pass energy, 50 meV step sizes, and 100 ms dwell times. Charge neutralization was used for all samples to reduce any potential differential charging effects. Data processing was performed with CasaXPS Version 2.3.15. High resolution core-level peaks were compared by normalizing counts for each respective core-level. Constrained fits were applied to evaluate differences between spectra. For Ni 2p peaks, the fitting was largely adapted from Grosvenor *et al.*¹¹

Thermal gravimetric analysis (TGA). A TA Instruments TGA Q500 instrument was used for TGA data acquisition. Films placed onto the pan were heated at a rate of 5 °C min⁻¹ and held isothermally at the final temperature (300 °C) for 30 min. Due to the small mass losses, all mass values were obtained after subtracting the mass loss observed from Ni foil background.

Thermogravimetric Analysis with Mass Spectrometry (TGA/MS). TGA with analysis of off-gas via MS was conducted using an STA 449 F3 Jupiter TGA (Netzsch Instruments, Selb, Germany) coupled to an HPR-20 MS (Hiden Analytical, Warrington, UK). The specimen was loaded into a platinum crucible, and was allowed to degas and stabilize in the TGA under flowing argon overnight prior to initiating the run. The MS was connected via a “T” to the vent from the TGA furnace and analyzed a continuous stream of gas during the TGA run. Due to the close coupling of the MS inlet to the TGA furnace, lag time between gas evolution from the specimen and its detection by MS was considered negligible on the time frame of the experiment and was ignored. The specimen was heated in the TGA at a rate of 5 °C min⁻¹ from 25 to 900 °C under a flow of 100 mL min⁻¹ ultra high purity (UHP) argon. The evolution of oxygen (m/z = 32) was monitored continuously by MS during the course of the TGA run. Due to the small sample size we estimate that TGA errors are 2% (relative) on mass changes.

Brunauer-Emmett-Teller (BET) Surface Area Analysis. Gas sorption experiments were performed on a Micrometrics ASAP 2020 Surface Area and Porosity Analyzer. Specimens were degassed at 100 °C for ~20 hours prior to analyses carried out at 77.35 K using UHP nitrogen as the adsorbate. The glass sample tubes had an inside diameter of 9.53 mm and the free space (volume) was measured prior to each experiment automatically, using UHP helium. Isotherms were measured over 87 total points - 48

adsorption points and 39 desorption points. Surface areas were calculated by the Brunauer-Emmett-Teller (BET) method using five adsorption points in the range $P/P_0 = 0.06$ to 0.2 .

Inductively Coupled Plasma Mass Spectrometry (ICP-MS). Samples were removed from the foil with mechanical means (e.g. by careful scraping with a razor blade or by bending the foil to release the sample) and then were digested in conc. HNO_3 (aq.) then diluted with DI water. Analysis was performed on a Perkin Elmer SCIEX Elan 6100 ICP-MS, calibrated with certified standards.

Electrochemical deposition

Electrochemical depositions of thin films were performed in a two-electrode cell connected to a Solartron Analytical SI 1287 Electrochemical Interface controlled by CorrWare electrochemical software. For Co_3O_4 films, the precursor solution was prepared following a procedure similar to those previously reported:^{1,2} $0.111 \text{ M Co}(\text{NO}_3)_2 \cdot 6\text{H}_2\text{O}$, 0.076 M NaNO_3 in 1:1 EtOH:deionized (DI) water. For all ratios of Ni-doped Co_3O_4 films, $\text{Ni}(\text{NO}_3)_2 \cdot 6\text{H}_2\text{O}$ was substituted in for $\text{Co}(\text{NO}_3)_2 \cdot 6\text{H}_2\text{O}$, maintaining the total metal ion concentration at 0.187 M . Ni foil was cleaned with detergent, rinsed with deionized water and acetone, and punched into discs of 15 mm diameter. The working electrode was comprised of a 15 mm diameter Ni foil disc secured in a flat specimen holder (K0105 Kit, Princeton Applied Research) and submerged in the precursor solution. The exposed surface area of the Ni foil in the assembly was 1 cm^2 . The auxiliary electrode was a large Pt foil square.

A current density of $-0.585 \text{ mA cm}^{-2}$ was applied (for 70 to 360 seconds, depending on the intended mass of deposition) resulting in a light blue-green film visible on the surface of the Ni foil. The sample was removed from the specimen holder, gently rinsed in deionized water and dried. Upon drying, the electrodeposited film (1 cm^2) was punched from the surrounding Ni substrate. The film was then placed in an alumina tray and ramped in a furnace (Thermo-Fisher) from room temperature to $300 \text{ }^\circ\text{C}$ over the course of two hours, followed by a two hour dwell period at $300 \text{ }^\circ\text{C}$. The oven was programmed to shut off following the dwell period, allowing the film to slowly cool to ambient temperature. The film had changed from blue-green to black in color.

Electrochemical Studies

Oxygen reduction studies were performed using a rotating disc electrode (RDE) assembly. RDE experiments were performed in a three-electrode cell connected to a Radiometer Analytical PGZ100 All-In-One Potentiostat. The rotation rate of the working electrode (EDI101, Radiometer Analytical), was controlled by a speed control unit (CTV101, Radiometer Analytical). For electrochemical analyses, the oxide films on Ni foil were housed in an adaptor [Radiometer Analytical, EM-EDI-SMP Disc Sample Holder Tip for EDI Rotating Disc Electrode (d=11 mm)] that was connected to the EDI101. The exposed geometric area of the film was 0.1963 cm^2 . The counter electrode was Pt and the reference electrode was Hg/HgO (0.1 M KOH, Hach, $E(\text{RHE}) = E(\text{Hg}/\text{HgO}) + 0.9351 \text{ V}$). The electrolyte was 0.1 M KOH solution that had been thoroughly purged with O_2 (ORR) or N_2 (ORR background, OER) for ≥ 20 minutes prior to the initiation of the experiment. The gaseous atmosphere was maintained for the duration of the experiment via blanketing. Linear scanning voltammograms were recorded from 0.2 V to -0.6 V vs. Hg/HgO for oxygen reduction studies. The working electrode was rotated in a series of discrete rotation rates (500, 900, 1600, 2500, 3600 rpm). Linear scanning voltammograms were recorded from 0 V to 1.2 V vs. Hg/HgO for oxygen evolution studies. The working electrode was rotated at either 1600 rpm or 2500 rpm. Stability and Chronoamperometric experiments were performed as described in the text, similar to recently published work.³⁻⁵

RDE experiments on $\text{Ni}_x\text{Co}_{3-x}\text{O}_4$ powders with Nafion and blends with Vulcan/Nafion were performed in a three-electrode cell, manufactured by Bioanalytical Systems, Inc. connected to a Versastat 4 potentiostat operated by VersaStudio software following methods described previously.³⁻⁵ Powders were obtained by mechanical removal of the spinel films. 40% Vulcan was found to be optimal. Electrodes (from BASi) included the glassy carbon working electrode (0.0788 cm^2), a Pt coil counter electrode, and a Ag/AgCl reference electrode (3 M NaCl, $E(\text{RHE}) = E(\text{Ag}/\text{AgCl}) + 0.9571$). RRDE experiments were performed in a three-electrode cell, manufactured by Gamry Instruments connected to a Gamry Series G 750 Test System Bipotentiostat. Electrodes included the Gamry RDE710 rotating working electrode prepared as described, Pt foil as the counter electrode, and a Hg/HgO reference electrode (0.1 M

KOH, Hach, $E(\text{RHE}) = E(\text{Hg}/\text{HgO}) + 0.9351 \text{ V}$) at a scan rate of 1 mV/s. RDE and RRDE experiments were not corrected for IR drop. n values (indicating the reaction order) were determined following published protocols⁶ The onset potential, typically defined as the potential at which the current first becomes negative, was alternatively defined in this study. The onset potential was determined from the averaged LSVs obtained at 2500 rpm, and was approximated from the intersection of a tangential line from 0 V and a tangential line from the half-wave potential. This approach likely underestimates the onset as compared to literature values in Table S3, but was found to be more reliable for relative comparisons across our samples here.

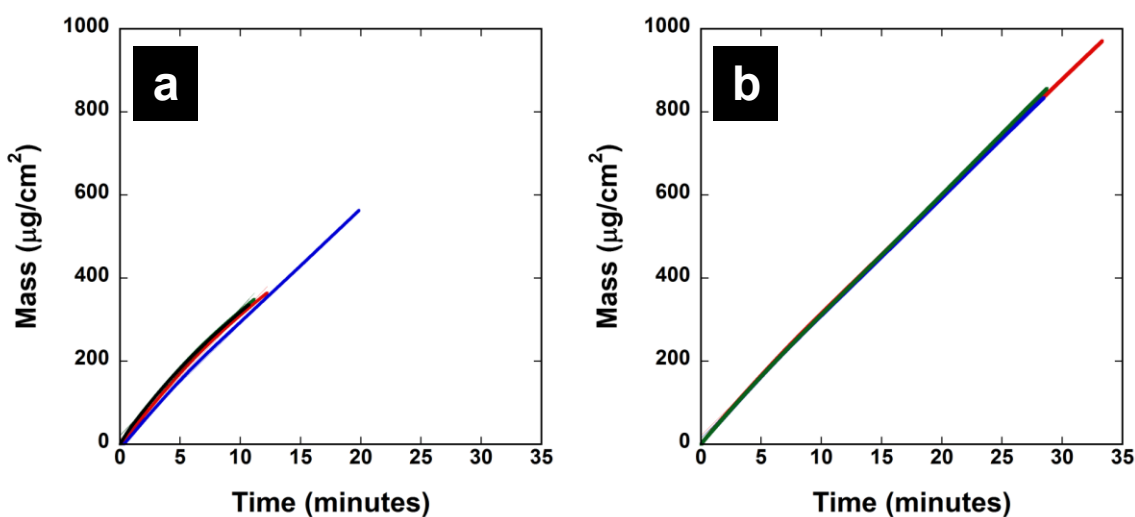


Figure S1. QCM data for electrodeposition from a) $\text{Co}(\text{NO}_3)_2 \cdot 6\text{H}_2\text{O}$ or b) $\text{Co}(\text{NO}_3)_2 \cdot 6\text{H}_2\text{O} : \text{Ni}(\text{NO}_3)_2 \cdot 6\text{H}_2\text{O}$ (with Co:Ni ratio = 1:0.5) solutions. Deposition rates of $29.94 \pm 1.13 \mu\text{g cm}^{-2} \text{ min}^{-1}$ (Co only) and $28.98 \pm 0.37 \mu\text{g cm}^{-2} \text{ min}^{-1}$ (Co:Ni ratio = 1:0.5) indicates that the inclusion of Ni in the solution has a minimal (if any) effect on the deposition rate.

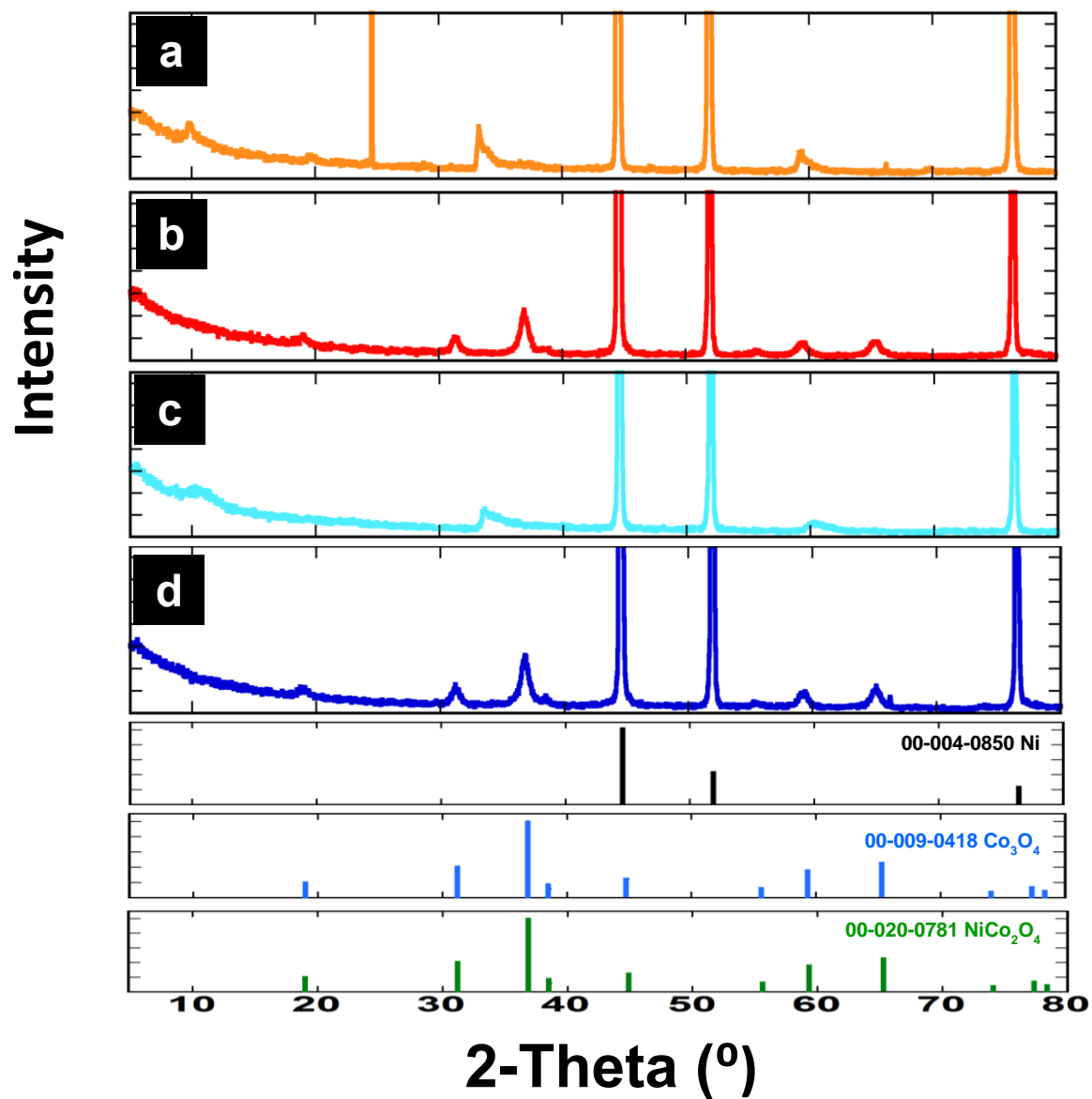


Figure S2. XRD spectra for a) $\text{Co}_1(\text{OH})_{2-x}(\text{NO}_3)_x \cdot y(\text{H}_2\text{O})$ and b) Co_3O_4 ; c) $\text{Ni}_z\text{Co}_{1-z}(\text{OH})_{2-x}(\text{NO}_3)_x \cdot y(\text{H}_2\text{O})$ and d) $\text{Ni}_x\text{Co}_{3-x}\text{O}_4$ from $\text{Co}:\text{Ni} = 1:0.5$. JCPDS file nos. 004-0850 (Ni), 009-0418 (Co_3O_4) and 020-0781 (NiCo_2O_4) are shown.

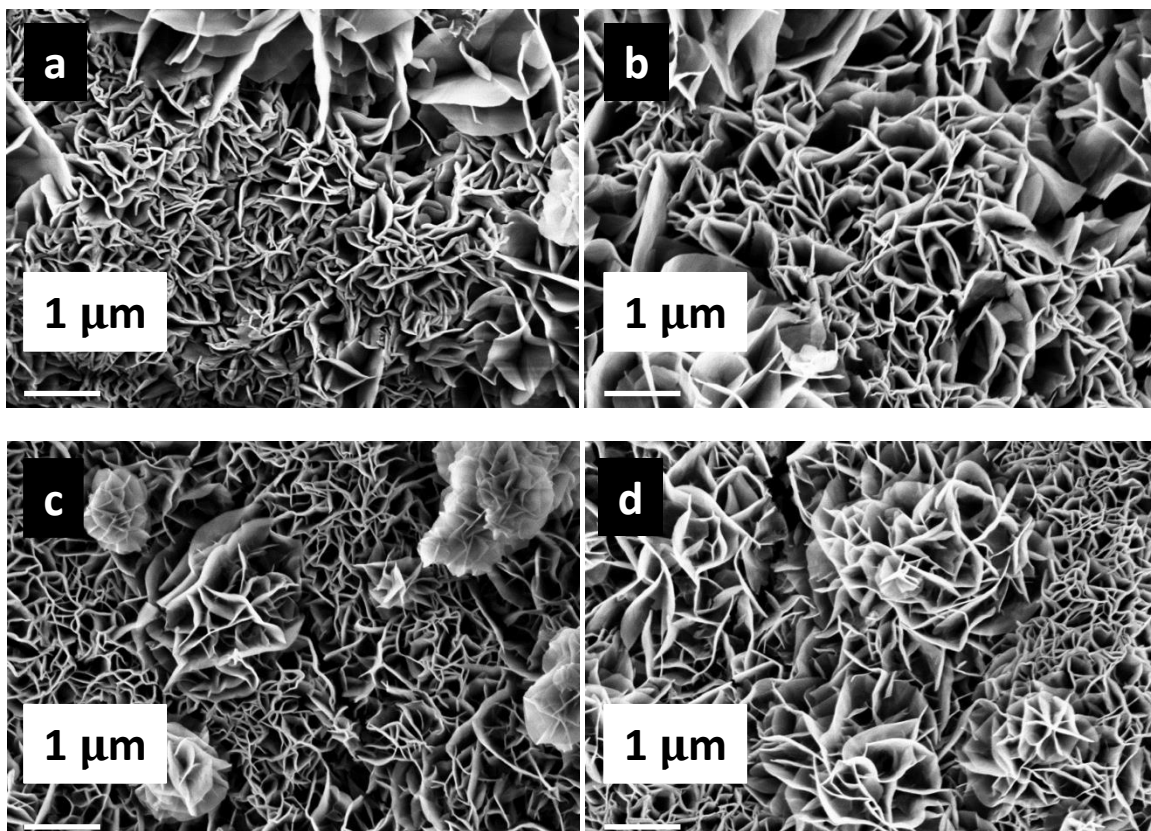


Figure S3. SEM images of a) $\text{Co}_1(\text{OH})_{2-x}(\text{NO}_3)_x \cdot y(\text{H}_2\text{O})$ and b) Co_3O_4 ; c) $\text{Ni}_z\text{Co}_{1-z}(\text{OH})_{2-x}(\text{NO}_3)_x \cdot y(\text{H}_2\text{O})$ and d) $\text{Ni}_x\text{Co}_{3-x}\text{O}_4$ (from Co:Ni = 1:0.5).

Table S1. Sample TGA analysis for conversion of $\text{Co}_1(\text{OH})_{2-x}(\text{NO}_3)_x \cdot y(\text{H}_2\text{O})$ and $\text{Co}_1-z\text{Ni}_z(\text{OH})_{2-x}(\text{NO}_3)_x \cdot y(\text{H}_2\text{O})$ films into Co_3O_4 or $\text{Ni}_x\text{Co}_{3-x}\text{O}_4$, respectively.

SAMPLE	INITIAL MASS, mg	FINAL MASS, mg (after cooling)	TOTAL MASS LOST, mg	TOTAL MASS LOST, μg	Ni baseline, μg lost	MASS LOST, μg	PERCENT MASS LOST	AVG PERCENT MASS LOST
Co_1	34.82556	34.7339	0.09166	91.66	18.89	72.77	27.56	26.02
Co_2	35.48953	35.40602	0.08351	83.51	18.89	64.62	24.48	
Co:Ni_1	34.09114	34.01309	0.07805	78.05	18.89	59.16	22.93	23.97
Co:Ni_2	34.33592	34.2525	0.08342	83.42	18.89	64.53	25.01	

Table S2. Effect of Cobalt:Nickel cation ratio in electrolyte solution on final spinel oxide film stoichiometry.

SAMPLE	Co:Ni (Precursor Solution)	Co:Ni (ICP-MS)	Stoichiometry (ICP-MS)	Reported In Manuscript as
Co_3O_4	1:0	297:1	Co_3O_4	Co_3O_4
$\text{Ni}_x\text{Co}_{3-x}\text{O}_4$ 1:0.25	1:0.25	5.77:1	$\text{Ni}_{0.44}\text{Co}_{2.56}\text{O}_4$	$\text{Ni}_{0.4}\text{Co}_{2.6}\text{O}_4$
$\text{Ni}_x\text{Co}_{3-x}\text{O}_4$ 1:0.5	1:0.5	4.08:1	$\text{Ni}_{0.59}\text{Co}_{2.41}\text{O}_4$	$\text{Ni}_{0.6}\text{Co}_{2.4}\text{O}_4$
$\text{Ni}_x\text{Co}_{3-x}\text{O}_4$ 1:1	1:1	2.39:1	$\text{Ni}_{0.89}\text{Co}_{2.11}\text{O}_4$	$\text{Ni}_{0.9}\text{Co}_{2.1}\text{O}_4$

Solubility vs. pH calculations for Co^{2+} and Ni^{2+} species.

Solubilities for Co and Ni were calculated using literature data.⁷ The relevant equations are:

$$\log[\text{Co}^{2+}] = 12.60 - 2\text{pH}$$

$$\log[\text{HCoO}_2^-] = -19.10 + \text{pH}$$

$$\log[\text{Ni}^{2+}] = 12.18 - 2\text{pH}$$

$$\log[\text{HNiO}_2^-] = -18.22 + \text{pH}$$

Summing the equations for each ionic species yields the lines in Figure S5.

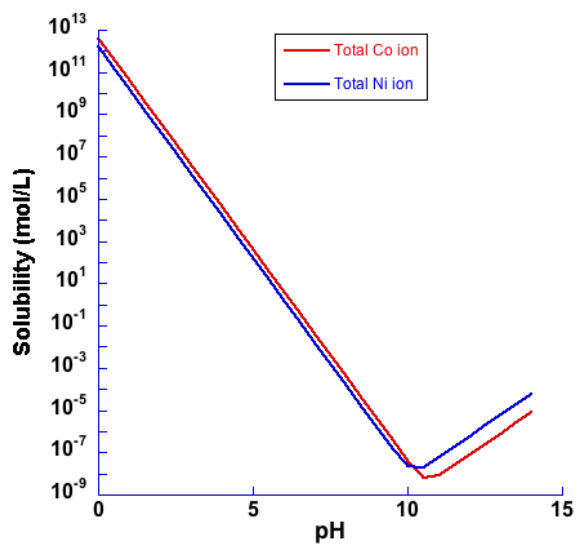


Figure S4. Calculated Solubility vs. pH for Co^{2+} and Ni^{2+} species.

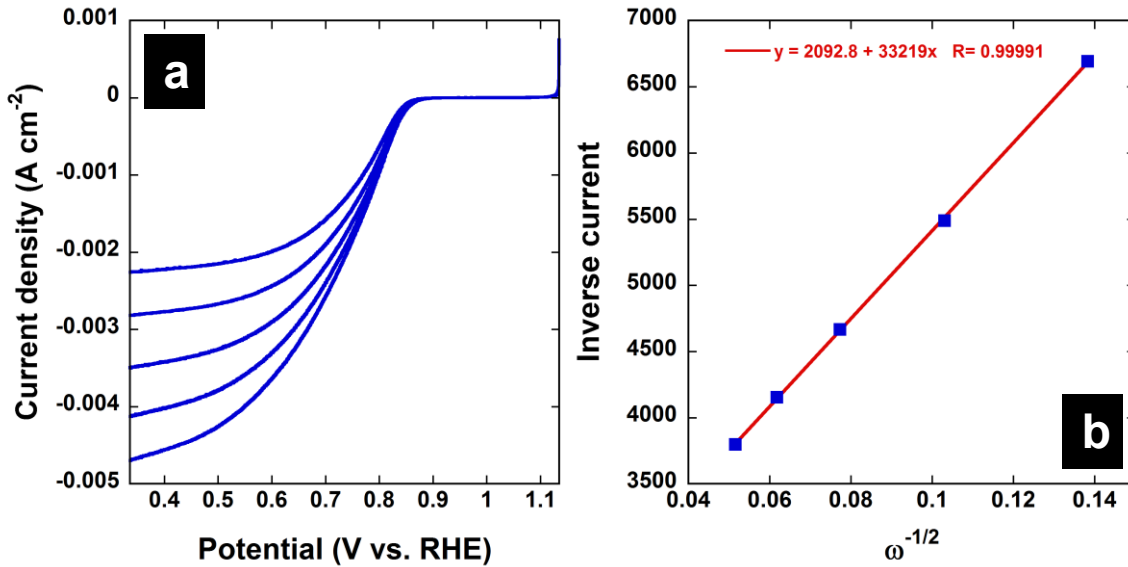


Figure S5. a) ORR polarization curves on Ni_{0.4}Co_{2.6}O₄ powder/Vulcan/Nafion electrocatalyst blend at discrete rotation rates: 500, 900, 1600, 2500, 3600 rpm (from top to bottom). b) Koutecky-Levich plot of inverse current vs. square root of the rotation rate, with a linear curve fit shown. The slope of this line is used in Koutecky-Levich calculations, below, which indicate a reaction order of $n = 3.89$.³⁻⁵

$$(j)^{-1} = (j_K)^{-1} + (B\omega^{1/2})^{-1}$$

$$B = 0.62nFC_0(D_0)^{3/2}v^{-1/6}$$

$$j_K = nFkC_0$$

$$\therefore n = [(0.62)(33219)FC_0AD^{2/3}v^{-1/6}]^{-1}$$

$$n = 3.89$$

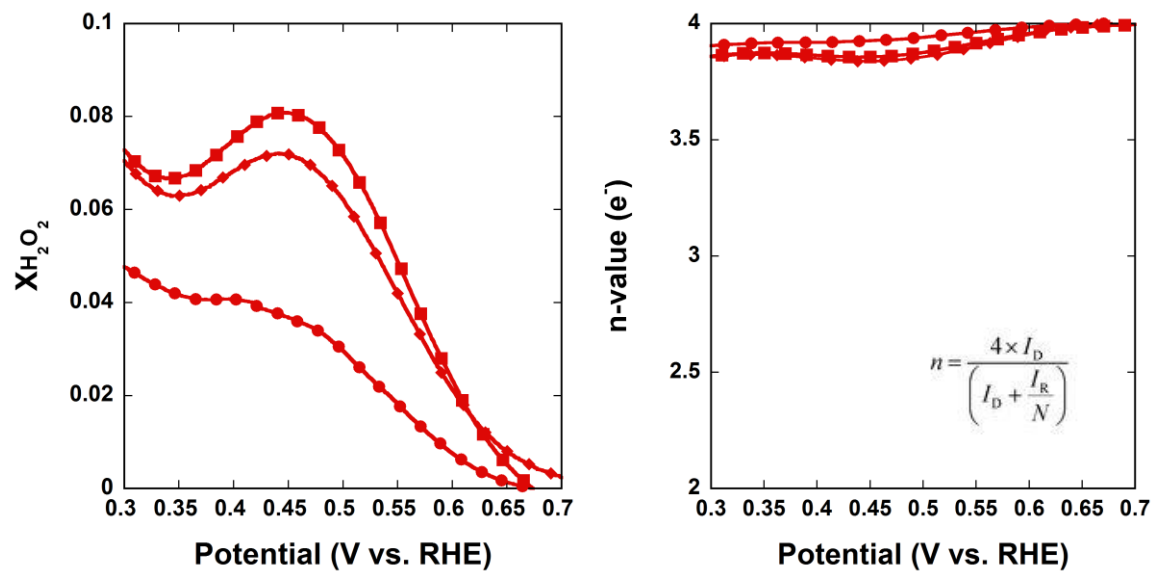


Figure S6. RRDE for three independent samples of $\text{Ni}_{0.6}\text{Co}_{2.4}\text{O}_4$ at 2500 rpm showing less than 8% peroxide formation from $\text{Ni}_x\text{Co}_{3-x}\text{O}_4$ and high n values. n values were calculated following published protocols, as recently reported.⁵

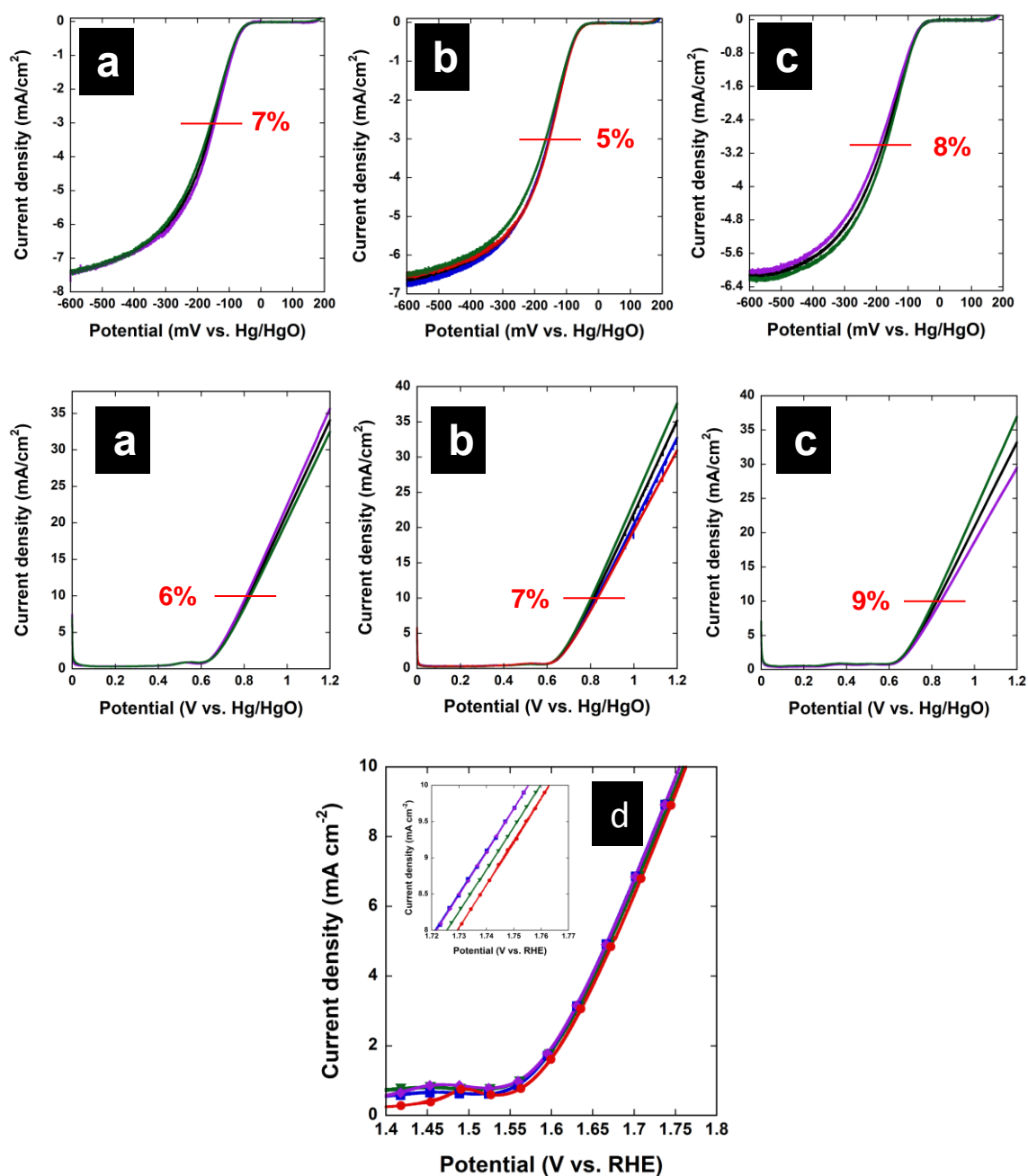


Figure S7. (top) ORR and (bottom) OER polarization curves for (a) Ni_{0.4}Co_{2.6}O₄, (b) Ni_{0.6}Co_{2.4}O₄, (c) Ni_{0.9}Co_{2.1}O₄ showing data for independent films (colored) as well as the average curve (black), as used in the main text. All samples are within 10% (width) of the average at the metric values of -3 mA/cm² for ORR and 10 mA/cm² for OER. d) Averaged OER 1600 RPM data showing Co₃O₄ (filled circles, red); Ni_{0.4}Co_{2.6}O₄ (filled diamonds, purple); Ni_{0.6}Co_{2.4}O₄ (filled squares, blue); Ni_{0.9}Co_{2.1}O₄ (filled triangles, dark green). Inset provides an expanded view of data approaching the 10 mA cm⁻² metric.

Table S3. Data comparison for OER/ORR Ni_xCo_{3-x}O₄ catalysts

Catalyst Material	Substrate - Preparation Method	Catalyst loading (mg cm ⁻²)	BET Surface Area (m ² g ⁻¹)	Stoichiometry (Co:Ni)	ORR: E(V) at I= -3 mA cm ⁻²	OER: E(V) at I = 10 mA cm ⁻²	Oxygen Electrode Δ(OER-ORR): E(V)	ORR Onset (V)	OER Onset (V)
Commercial Benchmarks									
20% Ir/C ^[51]	GC electrode	0.127	ND	NA	0.57	1.85	1.28	0.77	0.51
20% Pt/C ^[51]	GC electrode	0.127	ND	NA	0.75	NA	ND	0.91	1.64
20% Ir/C ^[52]	GC electrode	0.028	ND	NA	0.69	1.61	0.92	0.73	1.51
20% Pt/C ^[52]	GC electrode	0.028	ND	NA	0.86	2.02	1.16	0.98	1.66
Bifunctional Ni_xCo_{3-x}O₄									
1:0.25 Ni _x Co _{3-x} O ₄ ^[51]	Ni foil - ED, 300 °C in air	0.127	99.8	Ni _{0.4} Co _{2.6} O ₄	0.79	1.75	0.96	0.88	1.59
1:0.5 Ni _x Co _{3-x} O ₄ ^[51]	Ni foil - ED, 300 °C in air	0.127	94.2	Ni _{0.6} Co _{2.4} O ₄	0.78	1.76	0.98	0.88	1.57
1:1 Ni _x Co _{3-x} O ₄ ^[51]	Ni foil - ED, 300 °C in air	0.127	101.4	Ni _{0.9} Co _{2.6} O ₄	0.75	1.76	1.01	0.87	1.59
NiCo ₂ O ₄ Spinel NWAs ^[53]	GC electrode - HT 80 °C, 400 °C in air	ND	124	NiCo ₂ O ₄ (2:1)	0.75	1.72	0.97	0.84	1.65
OER Ni_xCo_{3-x}O₄									
Hollow Urchin-like Ni _x Co _{3-x} O ₄ ^[54]	GC electrode - HST 70 °C in air	0.069	117	NiCo ₂ O ₄ (2:1)	ND	1.63	ND	ND	1.55
NiCo ₂ O ₄ NWAs ^{**[55]}	FTO - HT 120 °C, 350 °C in air	ND	125.5	NiCo ₂ O ₄ (2:1)	ND	1.77	ND	ND	1.52
Ni-substituted Co ₃ O ₄ NWAs ^{***[56]}	Ni foam - HT 90 °C, 250 °C in air	ND	ND	Ni _{1.5} Co _{1.5} O ₄ (1:1)	ND	1.58	ND	ND	1.55
Ni _x Co _{3-x} O ₄ NWAs ^{***,ψ[57]}	Ti foil - HT 90 °C, 250 °C in air	ND	112	Ni _{0.71} Co _{2.29} O ₄	ND	1.61	ND	ND	1.56
ORR Ni_xCo_{3-x}O₄									
Hierarchical Urchin-like Ni _x Co _{3-x} O ₄ ^{*[58]}	GC electrode - HT 120 °C in air	0.35	122.8	NiCo ₂ O ₄	0.81	ND	ND	0.9	ND
Urchin-like Ni _x Co _{3-x} O ₄ Spheres ^[59]	GC electrode - HT 400 °C in air	1.2	92.3	NiCo ₂ O ₄	NA	ND	ND	0.83	ND
3-D Macroporous NiCo ₂ O ₄ ^[510]	GC electrode - HST 180 °C in air	0.804	26	NiCo ₂ O ₄ (2:1)	NA	ND	ND	0.86	ND
Carbon-supported Ni_xCo_{3-x}O₄									
NiCo ₂ O ₄ /PAN "NCO-A1" ^[511]	GC electrode - ES, 450 °C in air	0.899	ND	NiCo ₂ O ₄	0.78	1.62	0.84	0.87 (0.93)	1.54
Mesoporous NiCo ₂ O ₄ /Graphene ^[512]	GC electrode - HT 120 °C, 300 °C in air	0.407	77	NiCo ₂ O ₄	0.55	1.69	1.14	0.86 (0.87)	1.6
NiCo ₂ O ₄ /N-Graphene Paper ^[513]	N-G film - HST 90 °C, 250 °C in air	ND	155****	NiCo ₂ O ₄ (2:1)	ND	1.66	ND	ND	1.53

Table S3 Notes:

All Voltages (V) vs. RHE, *MOR performed, but no OER, ** Tested in 1M KOH, ***Tested in 1M NaOH, ^ψNi/Co = 0.31 ± 0.02 by ICP (i.e. Ni_{0.71}Co_{2.29}O₄) Ni/Co = 1.42 ± 0.01 by XPS (i.e. surface is enriched with Ni), ****By methylene blue absorption, GC = glassy carbon, ED = electrodeposition, HST (HT) = (Hydro)/solvothermal, ES = electrospun, NA = not attained, ND = not determined. Ir/C and Pt/C were newly purchased for our study. Attempts to activate the Ir/C or Pt/C in reducing atmospheres failed to increase their activity. Hence values for 20% Pt/C and 20% Ir/C from the literature (obtained from Ref [S2]) are also provided. The data shows our Ni_xCo_{3-x}O₄ electrocatalysts exhibit similar overall oxygen electrode activity to the more costly and rare 20% Ir/C and 20% Pt/C benchmark materials.

An additional comparison between catalyst Ni_{0.4}Co_{2.6}O₄ [$\Delta(\text{OER-ORR}) = 0.96$ V, this work], and the NCO-A1 catalyst [$\Delta(\text{OER-ORR}) = 0.84$ V, Ref S11], is warranted. NCO-A1 has a lower $\Delta(\text{OER-ORR})$ value but this work employed a very high total catalyst loading of 899 $\mu\text{g cm}^{-2}$. It is unknown how this catalyst would compare at lower loadings. A direct comparison of ORR half-wave mass activity can be made between NCO-A1 (-35.7 mA cm⁻² μg^{-1}), and Ni_{0.4}Co_{2.6}O₄ (-130 mA cm⁻² μg^{-1}). This indicates that the Ni_{0.4}Co_{2.6}O₄ catalyst here is roughly 3.6 times more efficient in the half-wave region than the NCO-A1 catalyst. Furthermore, this performance is achieved without the use of carbon, which can be problematic due to corrosion at OER potentials.

[S1] This work.

[S2] Y. Gorlin and T. F. Jaramillo, *J. Am. Chem. Soc.*, 2010, **132**, 13612-13614.

[S3] C. Jin, F. Lu, X. Cao, Z. Yang and R. Yang, *J. Mater. Chem. A*, 2013, **1**, 12170-12177.

[S4] J. Wang, T. Qiu, X. Chen, Y. Lu and W. Yang, *J. Power Sources*, 2014, **268**, 341-348.

[S5] X. Yu, Z. Sun, Z. Yan, B. Xiang, X. Liu and P. Du, *J. Mater. Chem. A*, 2014, **2**, 20823-20831.

[S6] B. Lu, D. Cao, P. Wang, G. Wang and Y. Gao, *Int. J. Hydrog. Energ.*, 2011, **36**, 72-78.

[S7] Y. Li, P. Hasin and Y. Wu, *Adv. Mater.*, 2010, **22**, 1926-1929.

[S8] P. Manivasakan, P. Ramasamy and J. Kim, *Nanoscale*, 2014, **6**, 9665-9672.

[S9] Z.-Q. Liu, Q.-Z. Xu, J.-Y. Wang, N. Li, S.-H. Guo, Y.-Z. Su, H.-J. Wang, J.-H. Zhang and S. Chen, *Int. J. Hydrogen Energ.*, 2013, **38**, 6657-6662.

[S10] Y. Xiao, C. Hu, L. Qu, C. Hu and M. Cao, *Chem. Eur. J.*, 2013, **19**, 14271-14278.

[S11] M. Prabu, K. Ketpang and S. Shanmugam, *Nanoscale*, 2014, **6**, 3173-3181.

[S12] D. U. Lee, B. J. Kim and Z. Chen, *J. Mater. Chem. A*, 2013, **1**, 4754-4762.

[S13] S. Chen and S.-Z. Qiao, *ACS Nano*, 2013, **7**, 10190-10196.

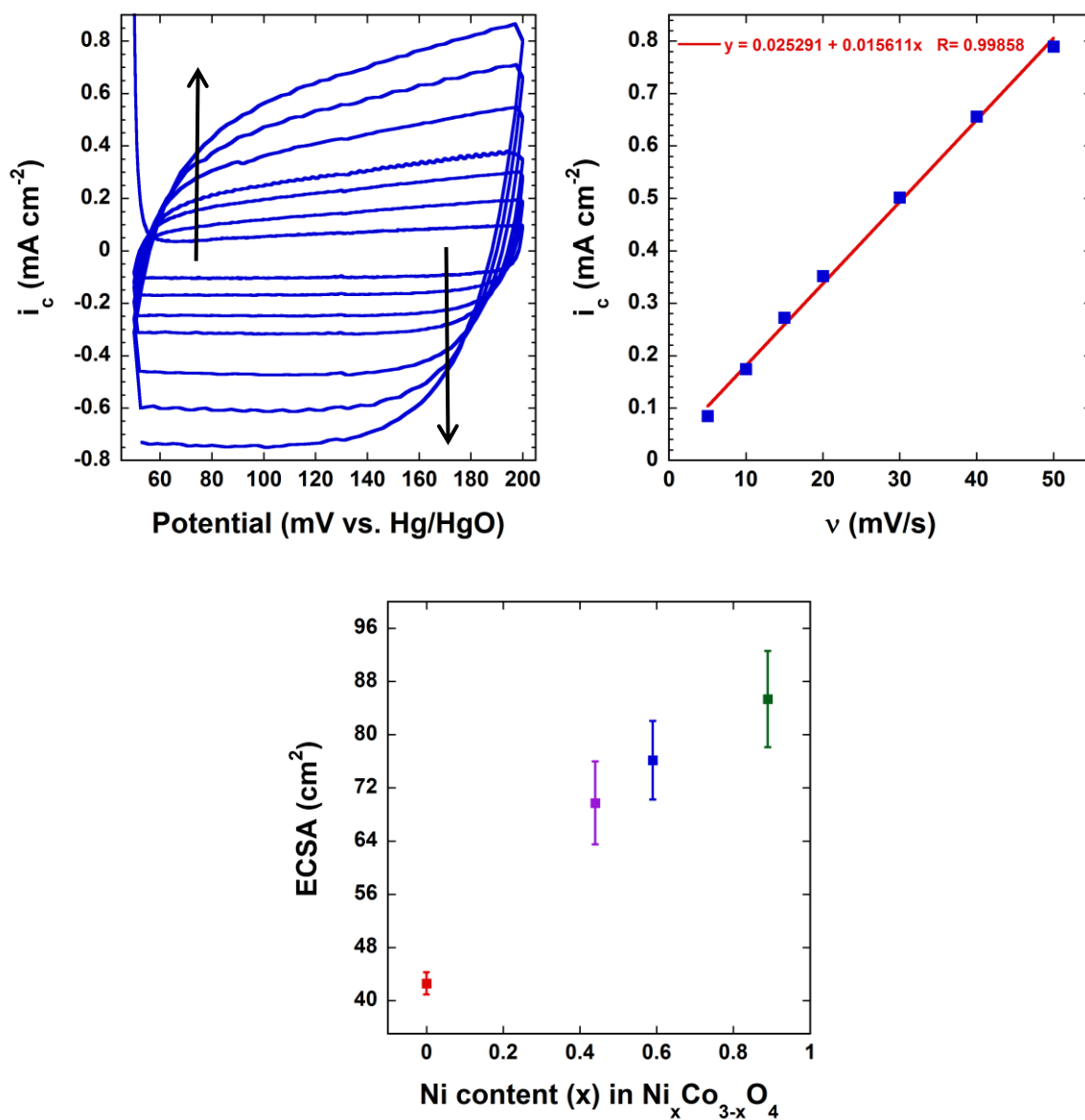


Figure S8. (top left) Representative cyclic voltammograms at discrete scan rates of 5, 10, 15, 20, 30, 40, 50 mV s^{-1} (in the direction of the arrows) for a $\text{Ni}_{0.4}\text{Co}_{2.6}\text{O}_4$ film. (top right) Linear curve fit for capacitive current vs. scan rate at 170 mV vs Hg/HgO (within 20% of $E_{\lambda,a}$). Double layer capacitance was found by multiplying the slope of this line (dependence of i_c on scan rate) by the geometric area, yielding $C_{dl} = 0.0027769$ F. Specific capacitance was defined as $C_s = 0.040$ mF cm^{-2} .⁸ (bottom) Averaged ECSA data. The error bars represent $\sim 95\%$ confidence level as determined from 2 x standard error mean ($= [s/\sqrt{n}]$), where s = sample standard deviation, n = size (number of observations) of the sample.^{9 a} as determined by ICP

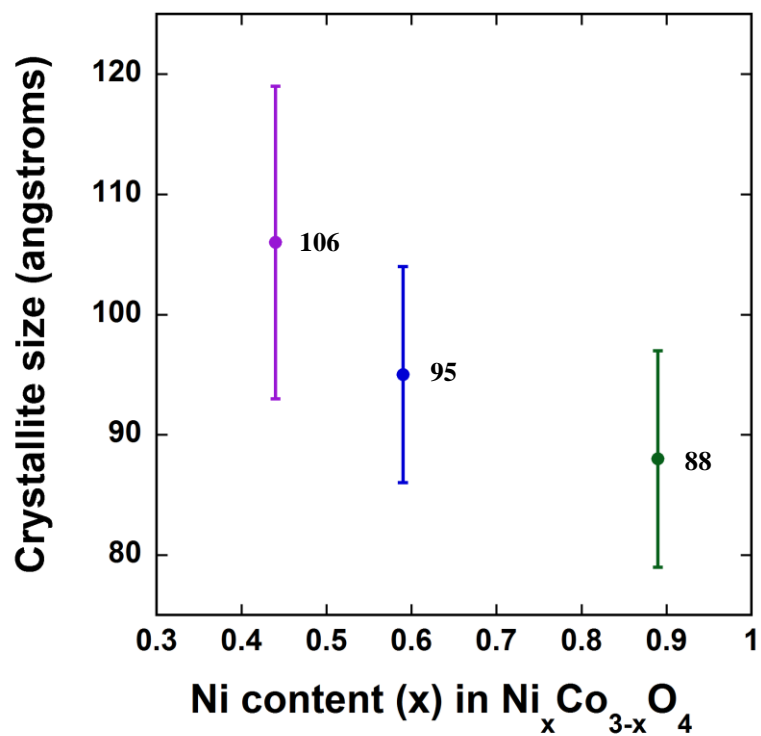


Figure S9. Scherrer XRD analysis (based on the 220 peak) showing average crystallite size as a function of stoichiometric Ni concentration (as determined by ICP-MS): Ni_{0.4}Co_{2.6}O₄ (purple), Ni_{0.6}Co_{2.4}O₄ (blue) and Ni_{0.9}Co_{2.1}O₄ (green). The error bars represent the obtained standard deviation.

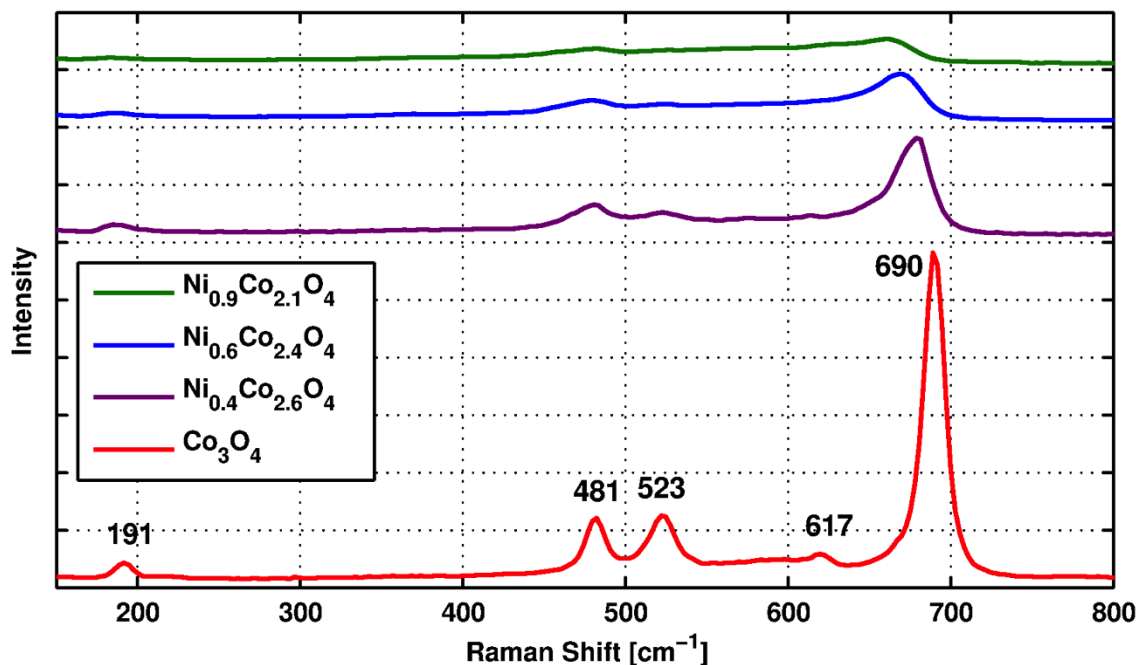


Figure S10. Representative Raman spectrum for each of the $\text{Ni}_x\text{Co}_{3-x}\text{O}_4$ films. Spectra are presented in their “raw” form to highlight reductions in intensity and broadening of modes that occur with larger amounts of nickel incorporation.

Raman spectroscopy was utilized to assess the relative cobalt concentration and crystal structure of the films. To this end, Figure S10 shows representative spectra of films having increasing Ni content acquired by averaging 3600 spectra over a $10 \times 10 \mu\text{m}$ area. Spectral resolution is $\pm 1 \text{ cm}^{-1}$. Spatial variation was minimal over all films. For the Co_3O_4 film having no Ni, 5 peaks are apparent having fitted positions of 191, 481, 523, 617 and 690 cm^{-1} . These are assigned to the F_{2g} , E_g , F_{2g} , F_{2g} and A_{1g} of Co_3O_4 , respectively.¹⁰ Compared to bulk Co_3O_4 , these peaks are within 3 cm^{-1} of literature values. All modes exhibit broader line-widths than that of their bulk counterparts indicative of crystalline disorder. With increasing amounts of Ni, the Raman spectrum changes in three distinct manners. First, the A_{1g} mode reduces in intensity. Second, the spectral region spanning $460\text{-}530 \text{ cm}^{-1}$ decreases in intensity. Third, the Raman modes broaden indicating reduced crystallite size with larger Ni content. Each of these spectral changes are consistent with that reported by Windisch *et al.* for films of $\text{Ni}_x\text{Co}_{3-x}\text{O}_4$, with $0 \leq x \leq 1$, that retain a predominately spinel type structure.¹¹ While indicative of a spinel

structure, Raman spectroscopy alone cannot rule out the presence of small regions of NiO. NiO exhibits a broad, weak, response from 480 to 660 cm^{-1} .^{12,13} This is the same region within which E_g and F_{2g} modes of $\text{Ni}_x\text{Co}_{3-x}\text{O}_4$ are present. Thus, the NiO signal, if present, could be overwhelmed by the spinel response of the $\text{Ni}_x\text{Co}_{3-x}\text{O}_4$. No spectral characteristic indicative of NiO was observed, however, within any of the films.

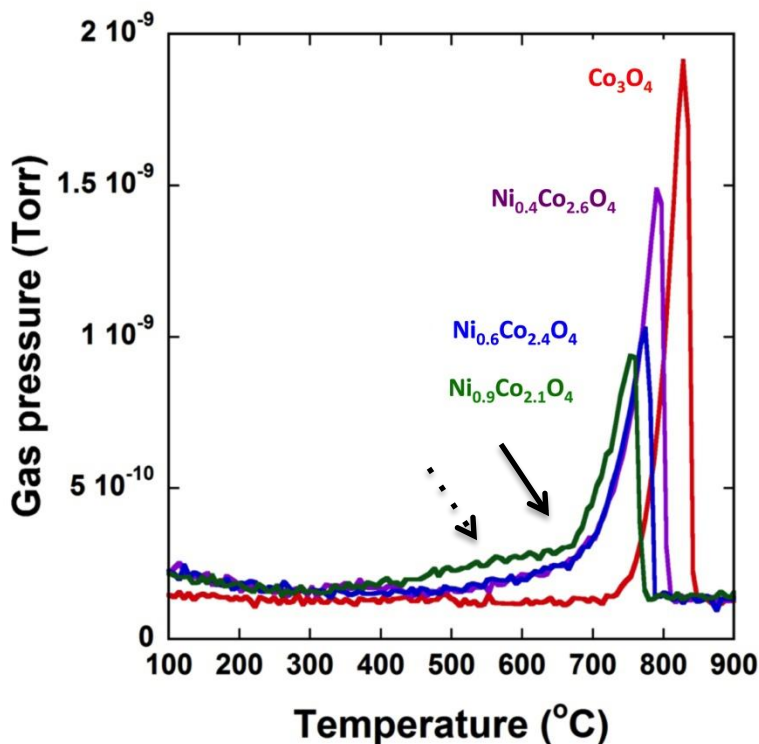


Figure S11. MS data acquired during TGA runs showing: the larger loss of O_2 (dashed arrow) from ~ 450 °C to ~ 650 °C, and earlier onset of Co_3O_4 to CoO transition (solid arrow), upon heating for higher values of x in $\text{Ni}_x\text{Co}_{3-x}\text{O}_4$. Mass losses (for relative comparison) from 25 °C to 650 °C were: 1.77% (Co_3O_4), 3.81% ($\text{Ni}_{0.4}\text{Co}_{2.6}\text{O}_4$), 4.40% ($\text{Ni}_{0.6}\text{Co}_{2.4}\text{O}_4$), 4.84% ($\text{Ni}_{0.9}\text{Co}_{2.1}\text{O}_4$)

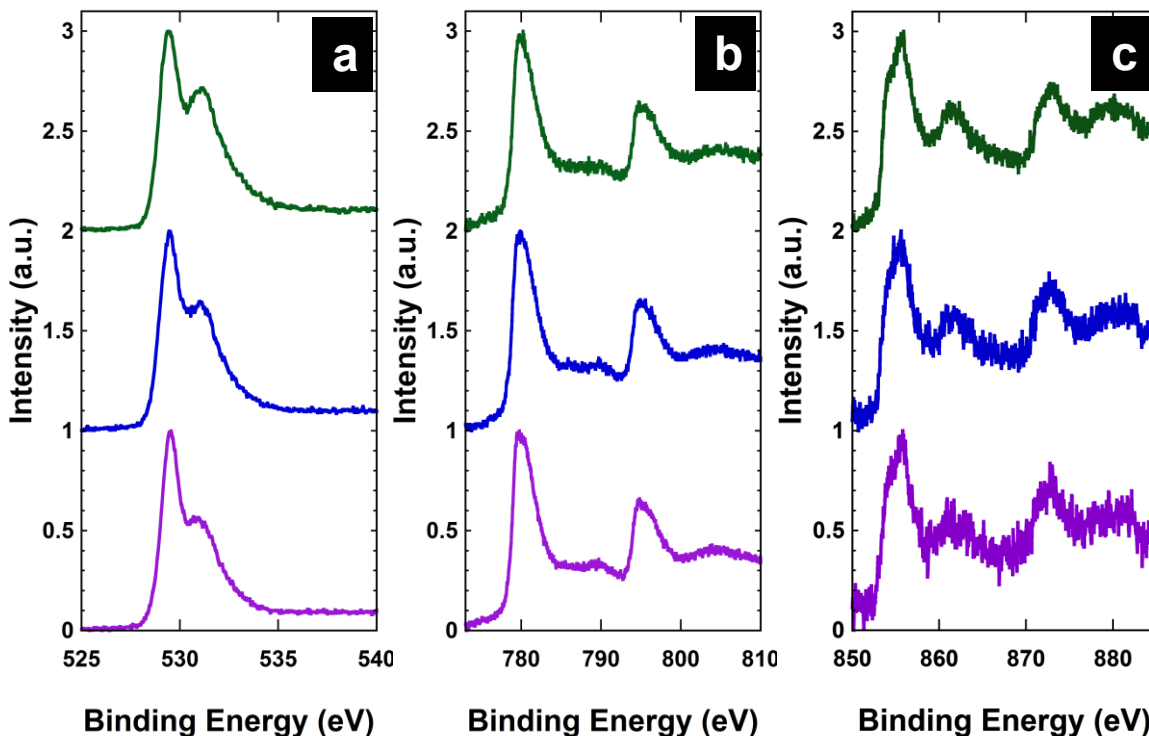


Figure S12. XPS data for $\text{Ni}_{0.4}\text{Co}_{2.6}\text{O}_4$ (purple), $\text{Ni}_{0.6}\text{Co}_{2.6}\text{O}_4$ (blue) and $\text{Ni}_{0.9}\text{Co}_{2.1}\text{O}_4$ (green): a) O 1s b) Co 2p c) Ni 2p.

XPS peak fitting and identification of oxidation states for Co 2p and Ni 2p have been discussed at length in the literature.¹⁴⁻¹⁸ Given the presence of strong satellite features, identification of oxidation states according to peak positions and/or shifts in the spectra is overly simplistic. XPS of standard nickel oxide based materials have shown that the entire spectral envelop may be different, or very similar, for different materials with different nickel oxidation states.¹⁵ Ni 2p peaks show the relative concentration at the surface increasing with more nickel in the spinel, as indicated by the increasing signal-to-noise ratio in Figure S11c. Very little difference could be observed in the Ni 2p peaks between samples. Co 2p peaks were also very similar for all samples. The O 1s peaks indicated an increase in relative hydroxide species with increasing nickel content.

References

1. J.-S. Do and R.-F. Dai, *J. Power Sources*, 2009, **189**, 204-210.
2. E. B. Castro, S. G. Real and L. F. Pinheiro Dick, *Int. J. Hydrogen Energ.*, 2004, **29**, 255-261.
3. T. N. Lambert, D. J. Davis, W. Lu, S. J. Limmer, P. G. Kotula, A. Thuli, M. Hungate, G. Ruan, Z. Jin and J. M. Tour, *Chem. Commun.*, 2012, **48**, 7931-7933.
4. D. J. Davis, A.-R. O. Raji, T. N. Lambert, J. A. Vigil, L. Li, K. Nan and J. M. Tour, *Electroanal.*, 2014, **26**, 164-170.
5. D. J. Davis, T. N. Lambert, J. A. Vigil, M. A. Rodriguez, M. T. Brumbach, E. N. Coker and S. J. Limmer, *J. Phys. Chem. C*, 2014, **118**, 17342-17350.
6. F. Cheng, Y. Su, J. Liang, Z. Tao and J. Chen, *Chem. Mater.*, 2010, **22**, 898-905.
7. M. Pourbaix, *Atlas of electrochemical equilibria in aqueous solutions*, Pergamon Press, Oxford, 1966.
8. C. C. L. McCrory, S. Jung, J. C. Peters and T. F. Jaramillo, *Journal of the American Chemical Society*, 2013, **135**, 16977-16987.
9. J. Gurland and R. C. Tripathi, *The American Statistician*, 1971, **25**, 30-32.
10. V. Hadjiev, M. Iliev and I. Vergilov, *J. Phys. C: Solid State Phys.*, 1988, **21**, L199-L201.
11. C. F. Windisch, G. J. Exarhos and R. R. Owings, *J. Appl. Phys.*, 2004, **95**, 5435-5442.
12. R. E. Dietz, G. I. Parisot and A. E. Meixner, *Phys. Rev. B*, 1971, **4**, 2302-2310.
13. J. E. Maslar, W. S. Hurst, W. J. Bowers, J. H. Hendricks and M. I. Aquino, *Corrosion*, 2002, **58**, 225-231.
14. J. G. Kim, D. L. Pugmire, D. Battaglia and M. A. Langell, *Appl. Surf. Sci.*, 2000, **165**, 70-84.
15. A. P. Grosvenor, M. C. Biesinger, R. S. C. Smart and N. S. McIntyre, *Surf. Sci.*, 2006, **600**, 1771-1779.
16. M. C. Biesinger, B. P. Payne, A. P. Grosvenor, L. W. M. Lau, A. R. Gerson and R. S. C. Smart, *Appl. Surf. Sci.*, 2011, **257**, 2717-2730.
17. R. D. L. Smith, M. S. Prévot, R. D. Fagan, S. Trudel and C. P. Berlinguette, *J. Am. Chem. Soc.*, 2013, **135**, 11580-11586.
18. C. F. Windisch, K. F. Ferris and G. J. Exarhos, *J. Vac. Sci. Technol. A*, 2001, **19**, 1647-1651.